J Mater Sci: Mater Electron (2014) 25:1908–1914
DOI 10.1007/s10854-014-1819-0

Effects of oxygen pressure on the microstructural, ferroelectric and magnetic properties of $BiFe_{0.95}Mn_{0.05}O_3$ thin films grown on Si substrates

W. Wang · Q. X. Zhu · M. M. Yang · R. K. Zheng · X. M. Li

Received: 17 December 2013 / Accepted: 18 February 2014 / Published online: 2 March 2014

Abstract We have investigated the effects of oxygen pressure on the microstructure, leakage current, ferroelectric and magnetic properties of $BiFe_{0.95}Mn_{0.05}O_3$ (BFMO) thin films epitaxially grown on $SrRuO_3$, $SrTiO_3$, and TiN-buffered (001)-oriented Si substrates. X-ray diffraction $\theta-2\theta$ scans and scanning electron microscope images reveal that the epitaxy and microstructures of the BFMO films were strongly dependent on oxygen pressure during film deposition. Epitaxial BFMO films can be obtained in a low oxygen pressure of 2 Pa while polycrystalline BFMO films were obtained in a relatively high oxygen pressure of 15 Pa. Furthermore, the oxygen pressure strongly influences the ferroelectric properties of the BFMO films grown on Si. The remnant polarization ($2P_r$) of approximately 107 $\mu C/cm^2$ and coercive field ($2E_c$) of approximately 580 kV/cm were observed for the epitaxial BFMO films grown in a low oxygen pressure of 2 Pa. The saturation magnetization of the BFMO films decreases with increasing oxygen pressure while the magnetic coercive field remains unchanged.

1 Introduction

Multiferroic materials with coexisting ferroelectric and magnetic orders have attracted intensive research interest in the past decade due to their potential applications in high density data storage, multistate logic, sensors, nonvolatile memories, and high-frequency microwave devices [1–3]. Perovskite $BiFeO_3$ (BFO) is one of the well-known single-phase materials that show antiferromagnetism with G-type magnetic structure below the Neel temperature $T_N \sim$ 643 K and ferroelectricity below the ferroelectric Curie temperature $T_C \sim 1{,}123$ K [4, 5]. BFO films usually exhibit a relatively high leakage current due to the reduction of a small portion of Fe^{3+} ions to Fe^{2+} ions, arising from the volatilization of Bi and oxygen deficiencies [6, 7]. Many efforts have been made to reduce the leakage current by introducing different dopants [8–10]. Partial substitution Fe for Mn is one of the most effective methods to improve the ferroelectric and magnetic properties [11, 12]. From the viewpoint of practical industrial applications, the growth of BFO films on Si substrates is particularly important since Si technology features a larger area, high volume and lower cost production. Much progress has been made in growing BFO films on Si substrates. The commonly used method was the direct growth of BFO films on commercial Pt, Ti, and SiO_2-buffered Pt/Ti/SiO_2/Si substrates [13–15]. Besides, BFO(001) films have been epitaxially grown on $SrRuO_3$/$SrTiO_3$/Si [16], $SrRuO_3$/CeO_2/YSZ/Si [17], and $SrRuO_3$/YSZ/Si substrates [16]. However, for the $SrRuO_3$/$SrTiO_3$/Si substrates, the $SrTiO_3$ layer has to be grown by molecular-beam epitaxy system while for the CeO_2/YSZ/Si and YSZ/Si substrates, the deposition conditions of YSZ layer on Si substrates are rigours. Therefore, it is highly desired to explore and grow epitaxial BFO films on Si substrates with the use of appropriate buffer layers.

In this paper, we report the epitaxial growth of $BiFe_{0.95}Mn_{0.05}O_3$ (BFMO) films on $SrRuO_3$ (SRO), $SrTiO_3$ (STO), and TiN-buffered Si(001) substrates by pulsed laser deposition and studied the influences of oxygen pressure

W. Wang · Q. X. Zhu · M. M. Yang · R. K. Zheng · X. M. Li (✉)
State Key Laboratory of High Performance Ceramics and Superfine Microstructures, Shanghai Institute of Ceramics, Chinese Academy of Sciences, Shanghai 200050, China
e-mail: lixm@mail.sic.ac.cn

W. Wang · Q. X. Zhu · M. M. Yang
Graduate University of Chinese Academy of Sciences, Beijing 100039, China

(P_{O_2}) on the microstructure, leakage current, ferroelectric and magnetic properties of the BFMO films. It was found that BFMO films could be epitaxially grown on such buffered Si(001) substrates at a substrate temperature of 570 °C and an appropriate P_{O_2} ($\sim$2 Pa). With increasing P_{O_2} from 2 to 15 Pa, the BFMO films become nanorod-like polycrystalline with discontinuous surface. The effects of P_{O_2} on the ferroelectric and ferromagnetic properties of the BFMO films are also discussed.

2 Experimental details

To compensate the volatilization of Bi during film deposition, a 15 % Bi-riched $Bi_{1.15}Fe_{0.95}Mn_{0.05}O_3$ (BFMO) ceramic target was used to fabricate BFMO films by pulsed laser deposition (PLD) using a KrF excimer laser (248 nm, Lamda Physik COMPexPro 201). Before the deposition of BFMO films, buffer layers composed of epitaxial SRO (50 nm), STO (25 nm), and TiN (10 nm) films were grown on HF-cleaned Si(001) substrates by laser molecular beam epitaxy. The SRO, STO, and TiN layers were grown at a substrate temperature of 700 °C and$P_{O_2} = 1 \times 10^{-4}$, 0.01, and 1 Pa with a repetition rate of 3 Hz and an energy density of 7, 4, 4 J/cm^2, respectively. BFMO films were then grown on such buffered Si(001) substrate by PLD with a repetition rate of 5 Hz and an energy density of 7 J/cm^2. During the growth of BFMO films, the substrate temperature was kept at 570 °C and P_{O_2} was fixed at 2, 10 and 15 Pa, respectively. After deposition, the BFMO films were in situ annealed in 1 atm O_2 at 570 °C for 30 min to reduce oxygen deficiencies and then cooled to room temperature at a rate of 6 °C/min.

Circular Pt top electrodes were deposited on the BFMO films by PLD through a shadow mask with a diameter of $\sim$100 μm in order to measure the electric and ferroelectric properties of the films. The phase purity and the epitaxial properties of the BFMO films with respect to the Si

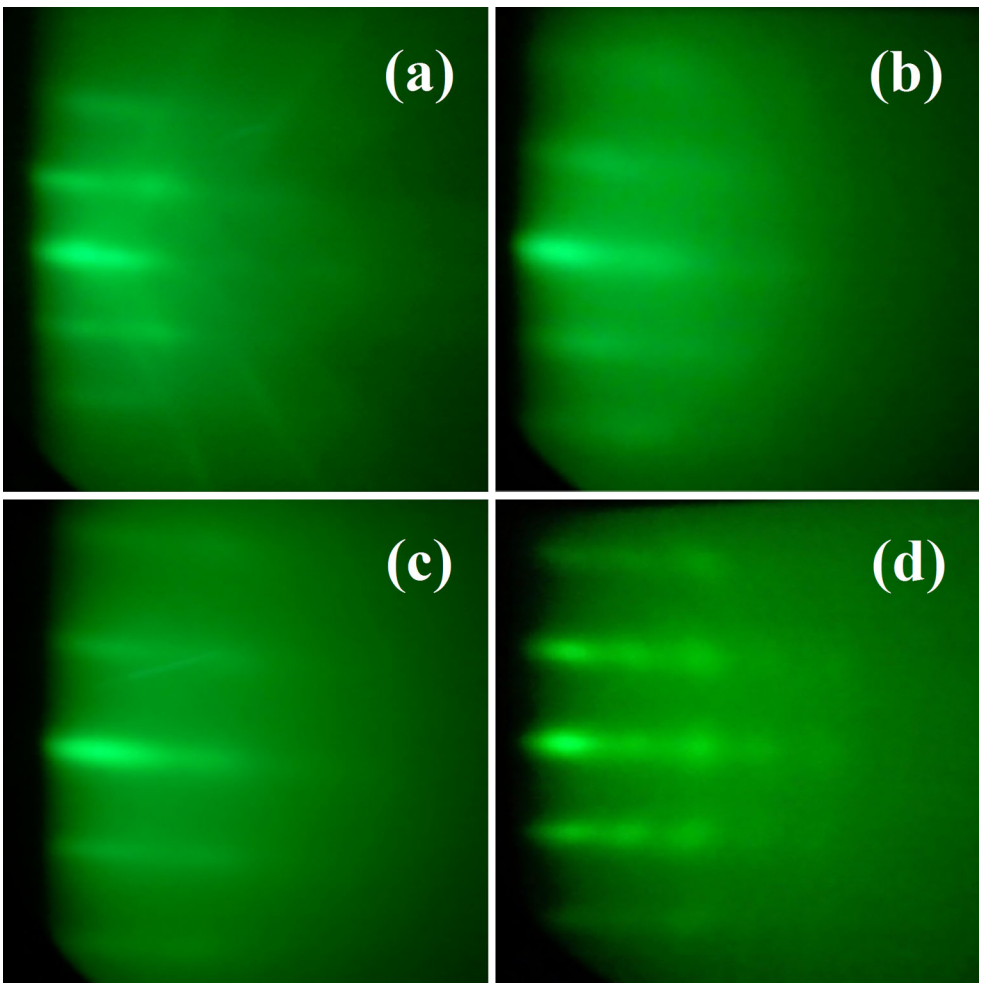

Fig. 1 In situ RHEED patterns obtained during the deposition of SRO, STO, and TiN buffer layers on Si(100). **a** Si substrate, **b** TiN on Si substrate, **c** STO on TiN film, **d** SRO on STO film

substrates were characterized by X-ray diffraction (XRD) $\theta-2\theta$ and ϕ-scans, respectively, using a high resolution four-circle Bruker D8 Discover X-ray diffractometer equipped with a 4-bounce Ge(220) monochromator and Cu Ka radiation (k = 1.5406 Å).

The microstructures of the BFMO films were examined using a Hitachi S-4800 field emission scanning electron microscope (FE-SEM). The ferroelectric and leakage current were measured by a Precision Multiferroic Analyzer (Radiant Technologies, Inc., USA) on a commercial probe station at room temperature. A superconducting quantum interference device (SQUID) magnetometer (MPMS XL-5, Quantum Design) was employed to measure the magnetic properties of the BFMO films with the magnetic field applied parallel to the film plane.

3 Result and discussion

The epitaxial growth of buffer layers on Si substrates was in situ monitored by reflection high-energy electron diffraction (RHEED). Figure 1a–d show the in situ RHEED patterns of the Si, TiN, STO, and SRO layers, respectively. Figure 1a shows the RHEED pattern of a HF-cleaned Si(100) substrate just before the deposition of the TiN layer. A symmetric sharp and streaky pattern can be clearly seen, implying clean and reconstructed surface of the Si(100) substrate. After growth of each layer, the sharp and streak pattern still appears (Fig. 1b, d) indicating epitaxial growth of the SRO layer on the STO layer, which will be further confirmed by XRD ϕ-scans.

Figure 2a shows the XRD $\theta-2\theta$ scans of the BFMO/SRO/STO/TiN/Si structure. Apparently strong BFMO(00l) (l = 1, 2, 3) diffraction peaks appear for the BFMO films deposited at different oxygen pressures. For BFMO films deposited at P_{O_2} = 2 Pa, besides the (00l) (l = 1, 2, 3) diffraction peaks, no other diffraction peaks were observed, suggesting that the BFMO film is of single phase and (001)-oriented. However, the BFMO films deposited at P_{O_2} = 15 Pa have weak BFMO (110) diffraction peak, indicating that this film has minor polycrystalline component. Note that a weak TiO_2 diffraction peak was observed at 2θ = 38°, which is probably due to minor oxidation of the TiN layer during the growth of STO layer on the TiN layer in the oxygen atmosphere (P_{O_2} = 0.01 Pa) [18]. We note that no diffraction peaks from the TiN, STO and SRO buffer layers were identified in the entire $\theta-2\theta$ scan region from 18° to 78°, which could be due to the similar lattice constants between the SRO and the BFMO films and the very thin layer of the TiN and STO. For BFMO films deposited at P_{O_2} = 10 Pa, diffraction peaks from Bi_2O_3 near 2θ = 31.1° and 32.8° were detected, which usually appears for BFMO films deposited at high oxygen pressure [19]. Figure 2b shows the in-plane XRD $\theta-2\theta$ scan of the BFMO/SRO/STO/TiN/Si structure where the BFMO film was deposited at P_{O_2} = 2 Pa. The in-plane epitaxial relationship between the BFMO film and the Si substrate was examined through XRD ϕ-scan taken on the BFMO, SRO and Si (111) diffraction peaks, respectively. Three sets of fourfold symmetrical diffraction peaks originating from the BFMO and SRO films and the Si substrate were observed (the insets of Fig. 2b), indicating the epitaxial nature of the BFMO film on the Si substrate. Such epitaxial growth of BFMO film on buffered Si substrate could be due to the good domain match between the TiN and Si, TiN and STO [20] as well as similar lattice constants among the STO, SRO and BFMO. The in-plane lattice constant a of the BFMO film, calculated from the in-plane and out-plane $\theta-2\theta$ scan data, is 3.95 Å,

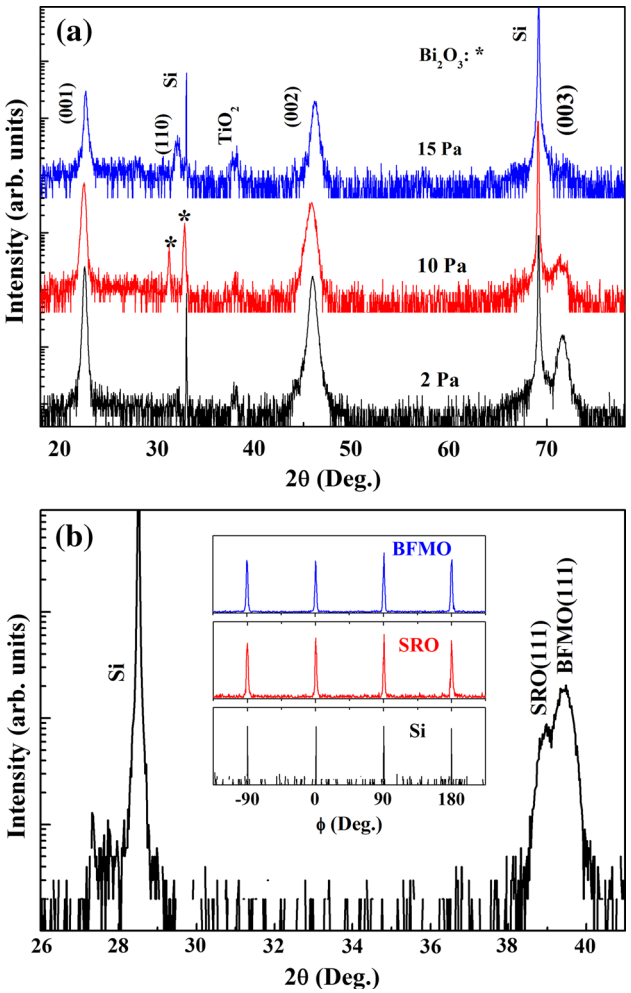

Fig. 2 **a** XRD $\theta-2\theta$ scan pattern of the BFMO thin films deposited on SRO, STO, and TiN-buffered (001) Si substrates at different oxygen pressure. The *asterisk* represents the Bi_2O_3 impurity phase. **b** In-plane XRD $\theta-2\theta$ scan of the BFMO/SRO/STO/TiN/Si structure with the BFMO thin films deposited at an oxygen atmosphere of 2 Pa. The *insets* show the XRD phi scan patterns of the BFMO(111), SRO(111) and Si(111) planes, respectively

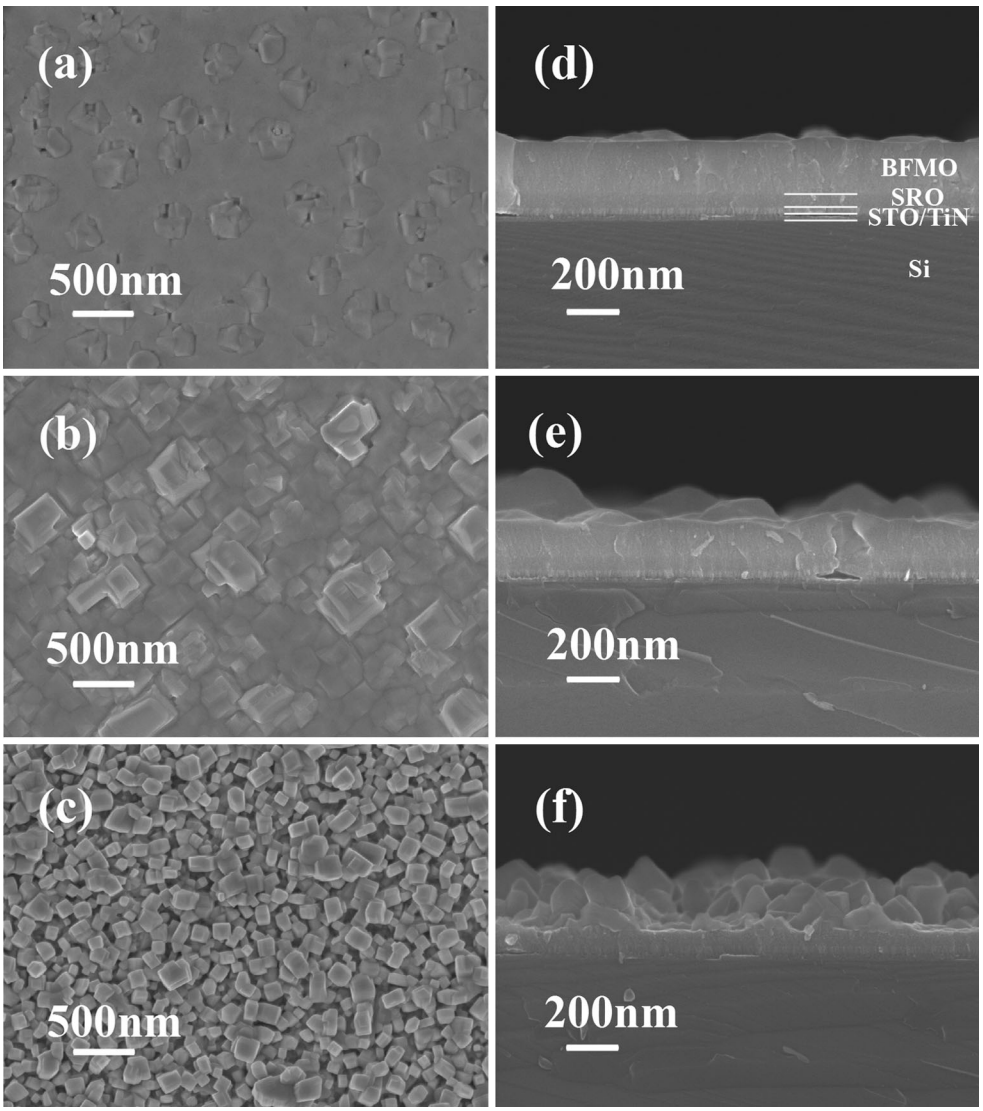

Fig. 3 Surface and cross-sectional FE-SEM images of BFMO thin films deposited at **a**, **d** 2 Pa, **b**, **e** 10 Pa and **c**, **f** 15 Pa

which is almost the same as that of the BFMO bulk ($a \sim b \sim c \sim 3.96$ Å) [21], revealing that the BFMO film is approximately strain free.

Figure 3 shows the surface and cross-sectional FE-SEM images of BFMO films deposited at $P_{O_2} = 2$, 10, and 15 Pa, respectively. It can be seen that the BFMO film deposited at $P_{O_2} = 2$ Pa and a substrate temperature of 570 °C shows smooth surface (Fig. 3a) and dense microstructure with a thickness of ~200 nm (Fig. 3d). In contrast, the BFMO film deposited at higher oxygen pressure ($P_{O_2} = 10$ Pa) (Fig. 3b, e) have a rough surface covered by square out-growths having ~500 nm in lateral size and ~60 nm in height. The corresponding XRD pattern for this film (cf. Fig. 2a, 10 Pa) shows additional diffraction peaks, which arises from the Bi_2O_3 phases. These phases segregate to the surface in self-organized arrays of squared-shaped outgrowths [22, 23]. With increasing oxygen pressure to 15 Pa, the BFMO film exhibits a discontinuous nanorod-like microstructure with a height of ~200 nm (Fig. 3c, f). The randomly oriented nanorods indicates the polycrystalline growth of the BFMO film.

Figure 4a shows the polarization–electric field (P–E) hysteresis loops of the Pt/BFMO/SRO capacitor where the BFMO film was deposited at $P_{O_2} = 2$ Pa. The measurements were carried out at room temperature at a frequency of 10 kHz. Figure 4c shows the electric field dependence of the P_r and E_c values for this capacitor. A square-like hysteresis loop with a remanent polarization ($2P_r$) of ~107 μC/cm^2 and coercive field ($2E_c$) of ~580 kV/cm were obtained for the (001)-oriented epitaxial BFMO film deposited at $P_{O_2} = 2$ Pa. The $2P_r$ of the epitaxial BFMO thin film is similar to that of BFO films grown on $SrTiO_3$ or Si substrate

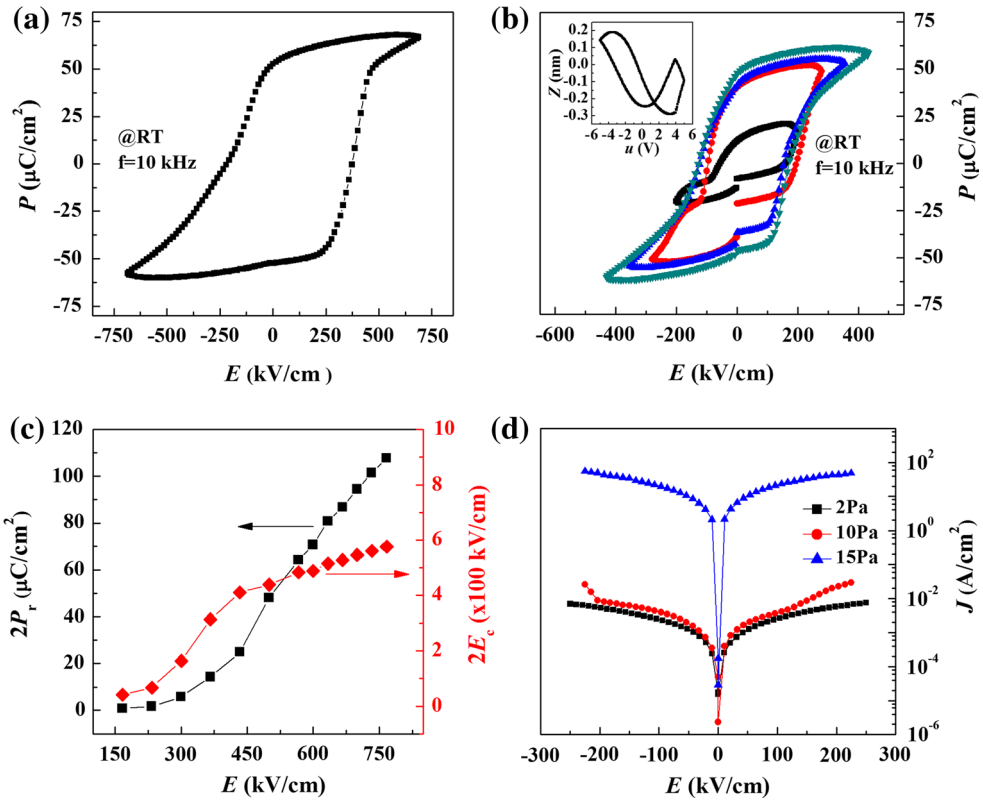

Fig. 4 Polarization–electric field (*P–E*) hysteresis loops for the Pt/BFMO/SRO structure with the BFMO thin films deposited at **a** 2 Pa, **b** 10 Pa, the *inset* in **b** shows the piezoresponse curve of BFMO thin films deposited at 15 Pa. **c** The electric field dependence of the P_r and E_c values for the BFMO thin films deposited at 2 Pa. **d** The leakage current density–electric field characteristics of BFMO thin films measured at RT

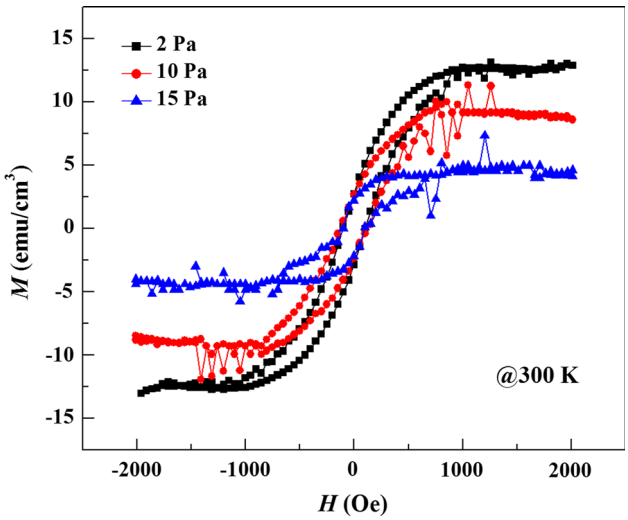

Fig. 5 Magnetization–magnetic field (*M–H*) hysteresis curves of BFMO films deposited at different oxygen pressures measured with an applied magnetic field of 2 kOe at 300 K

[16, 24, 25]. We note that the BFMO films deposited $P_{O_2} = 15$ Pa did not show any polarization hysteresis loops due to the large leakage current density in the film (shown in Fig. 4d). To check the ferroelectric property of the BFMO film deposited at $P_{O_2} = 15$ Pa, piezoresponse curve was measured. Butterfly-shaped curve was obtained (shown in inset of Fig. 4b), revealing local ferroelectric activity of the BFMO film deposited at $P_{O_2} = 15$ Pa. Although the 200-nm-thick BFMO film deposited at $P_{O_2} = 10$ Pa show good hysteresis loop (Fig. 4b) with large $2P_r$ of 93 μC/cm^2 and $2E_c$ of 300 kV/cm at $E = 430$ kV/cm, the measurement results were not stable and could not be repeated in some other samples deposited at the same conditions because of the uncontrollable distribution of Bi_2O_3 outgrowths.

Figure 5 shows the room-temperature magnetization-magnetic field (*M–H*) hysteresis loops of the BFMO films deposited at different oxygen pressures. Note that the diamagnetic signals from the Si substrate have been subtracted. The contribution of magnetization from the SRO film was neglected since the Curie temperature of SRO (~160 K) is much lower than room temperature. It can be seen that the bare BFMO film show a saturated weak ferromagnetic hysteresis loop at room temperature. The saturated magnetization (M_s) and coercive field (H_c) of the epitaxial BFMO films deposited under $P_{O_2} = 2$ Pa are ~12 emu/cm^3 and ~100 Oe, respectively. With increasing oxygen pressure, the M_s decreases to ~8.6 emu/cm^3 for films grown under 10 Pa and to ~4.1 emu/cm^3 for polycrystalline films grown under $P_{O_2} = 15$ Pa. No significant change in the coercive field was observed. M_s of the epitaxial BFMO films is comparable to those values for (001)-oriented $BiFe_{0.95}Mn_{0.05}O_3$ thin films grown on STO substrates [26] and higher than some other reports [27, 28].

Compared with the pure (001)-oriented BFO films ($M_s \sim 6.15$ emu/cm^3) [29] with similar thickness, the doping of Mn ions results in a much lower leakage current in the BFMO film in high electric field regions, which disfavors the double-exchange (DE) interaction since the DE interaction needs active hopping of charge carriers. Therefore, local ferromagnetic ordering in the antiferromagnetic ground state via DE interaction seems inadequate to explain the enhanced magnetization for the BFMO film. Compared with the $BiFeO_3$ films, the considerable enhancement in the magnetization associated with Mn doping is largely due to the increased spin canting [29]. However, it is quite complicated to explain the change of M_s with the increment of oxygen pressure during deposition. Generally, it was believed that M_s of BFMO films depends on the Bi/Fe ratio in BFMO film [19] and the valence state of the Fe and/or Mn ions associated with the oxygen vacancies in the films [30, 31]. As mentioned above, the M_s of BFMO thin films grown at $P_{O_2} = 2$ Pa was comparable to (or higher than) that of BFO and BFMO reported earlier [29, 32]. Therefore, it is believed that besides the oxygen vacancies which would partially reduce a portion of Fe^{3+} ions to Fe^{2+} ions [6, 33], the exchange coupling of Fe–O–Mn may also have an effect on the M_s [30].

4 Conclusions

BFMO thin films have been epitaxially grown on $SrRuO_3$, $SrTiO_3$, and TiN-buffered and (001)-oriented Si substrates by pulsed laser deposition at different oxygen pressures. X-ray diffraction $\theta-2\theta$ scans and SEM images reveal that the orientation and microstructure of BFMO films strongly depend on the oxygen pressures during film deposition. It was found that epitaxial BFMO thin films could be obtained in low oxygen pressure of 2 Pa while nanorod-like polycrystalline BFMO were found in high oxygen pressure of 15 Pa. The remanent polarization ($2P_r$) of approximately 107 μC/cm^2 and coercive field ($2E_c$) of approximately 580 kV/cm were obtained at an applied electric field of 700 kV/cm for the epitaxial BFMO films grown at $P_{O_2} = 2$ Pa. All BFMO films deposited at different oxygen pressures exhibit saturated *M–H* hysteresis loop, showing weak ferromagnetism. M_s of BFMO thin films increases with decreasing oxygen pressures, which is attributed to partial reduction of Fe^{3+} at low oxygen pressure and the exchange coupling of Fe–O–Mn.

Acknowledgments This work was supported by the NSFC (Grant Nos. 11090332, 51172259) and the CAS/SAFEA International Partnership Program for Creative Research Teams.

References

1. W. Eerenstein, N.D. Mathur, J.F. Scott, Nature **442**, 759–765 (2006)
2. R. Ramesh, N.A. Spaldin, Nat. Mater. **6**, 21–29 (2007)
3. G. Catalan, J.F. Scott, Adv. Mater. **21**, 2463–2485 (2009)
4. P. Fischer, M. Polomska, I. Sosnowska, M. Szymanski, J. Phys. C: Solid St. Phys. **13**, 1931–1940 (1980)
5. G.A. Smolenskiĭ, I.E. Chupis, Sov Phys Uspekhi **25**, 475–493 (1982)
6. W. Eerenstein, F.D. Morrison, J. Dho, M.G. Blamire, J.F. Scott, N.D. Mathur, Science **307**, 1203a (2005)
7. X. Qi, J. Dho, R. Tomov, M.G. Blamire, J.L. MacManus-Driscoll, Appl. Phys. Lett. **86**, 062903 (2005)
8. T. Kawae, Y. Terauchi, H. Tsuda, M. Kumeda, A. Morimoto, Appl. Phys. Lett. **94**, 112904 (2009)
9. J.G. Wu, J. Wang, D.Q. Xiao, J.G. Zhu, AIP. Adv. **1**, 022138 (2011)
10. T. Kawae, H. Tsuda, A. Morimoto, Appl. Phys. Express **1**, 051601 (2008)
11. S.K. Singh, H. Ishiwara, K. Maruyama, Appl. Phys. Lett. **88**, 262908 (2006)
12. K. Takahashi, M. Tonouchi, Jpn. J. Appl. Phys. **45**, L755–L757 (2006)
13. J. Wu, J. Wang, D. Xiao, J. Zhu, Appl. Surf. Sci. **258**, 1390–1394 (2011)
14. D. Li, X. Sun, X. Chuai, Z. Wu, Z. Cao, Y. Yan, D. Zhang, J. Cryst. Growth. **338**, 85–90 (2012)
15. X.M. Chen, G.D. Hu, J.C. Wang, L. Cheng, C.H. Yang, W.B. Wu, J. Alloy, Compound **509**, 431–434 (2011)
16. J. Wang, H. Zheng, Z. Ma, S. Prasertchoung, M. Wuttig, R. Droopad, J. Yu, K. Eisenbeiser, R. Ramesh, Appl. Phys. Lett. **85**, 2574–2576 (2004)
17. Z. Hu, M. Li, Y. Zhu, S. Pu, X. Liu, B. Sebo, X. Zhao, S. Dong, Appl. Phys. Lett. **100**, 252908 (2012)
18. W. Zhang, A. Chen, F. Khatkhatay, C.-F. Tsai, Q. Su, L. Jiao, X. Zhang, H. Wang, Acs. Appl. Mater. Interface **5**, 3995–3999 (2013)
19. L. You, N.T. Chua, K. Yao, L. Chen, J. Wang, Phys. Rev. B. **80**, 024105 (2009)
20. S. Mal, T.-H. Yang, P. Gupta, J.T. Prater, J. Narayan, Acta. Mater. **59**, 2526–2534 (2011)
21. F. Yan, T.J. Zhu, M.O. Lai, L. Lu, J. Appl. Phys. **110**, 084102 (2011)
22. H. Béa, M. Bibes, A. Barthélémy, K. Bouzehouane, E. Jacquet, A. Khodan, J.P. Contour, S. Fusil, F. Wyczisk, A. Forget, D. Lebeugle, D. Colson, M. Viret, Appl. Phys. Lett. **87**, 072508 (2005)
23. H. Béa, M. Bibes, S. Fusil, K. Bouzehouane, E. Jacquet, K. Rode, P. Bencok, A. Barthélémy, Phys. Rev. B. **74**, 020101 (2006)
24. J. Wang, J.B. Neaton, H. Zheng, V. Nagarajan, S.B. Ogale, B.T. Liu, D. Viehland, V. Vaithyanathan, D.G. Schlom, U.V. Waghmare, N.A. Spaldin, K.M. Rabe, M. Wuttig, R. Ramesh, Science **299**, 1719–1722 (2003)
25. J. Li, J. Wang, M. Wuttig, R. Ramesh, N. Wang, B. Ruette, A.P. Pyatakov, A.K. Zvezdin, D. Viehland, Appl. Phys. Lett. **84**, 5261–5263 (2004)
26. X.Q. Zhao, W. Wang, C. Zheng, Q.X. Zhu, X.M. Li, R.K. Zheng, J. Mater. Sci. Mater. Electron. **24**, 1677–1684 (2013)
27. J.Z. Huang, Y. Wang, Y. Lin, M. Li, C.W. Nan, J. Appl. Phys. **106**, 063911 (2009)
28. J.J. Gu, G.L. Zhao, F.W. Cheng, J.R. Han, L.H. Liu, H.Y. Sun, Phys. B. **406**, 4400–4403 (2011)
29. J. Wu, J. Wang, J. Appl. Phys. **106**, 054115 (2009)

30. K. Katsube, T. Matsui, H. Yamamoto, Y. Baba, N. Hirao, A. Iwase, J. Appl. Phys. **105**, 07D904 (2009)
31. R. Nechache, C. Harnagea, L.-P. Carignan, O. Gautreau, L. Pintilie, M.P. Singh, D. Ménard, P. Fournier, M. Alexe, A. Pignolet, J. Appl. Phys. **105**, 061621 (2009)
32. S. Gupta, A. Sharma, M. Tomar, V. Gupta, M. Pal, R.Y. Guo, A. Bhalla, J. Appl. Phys. **111**, 064110 (2012)
33. A. Ravalia, M. Vagadia, P. Trivedi, P.S. Solanki, K. Asokan, S. Ojha, O.P. Thakur, R.J. Choudhary, D.M. Phase, D.G. Kuberkar, Solid. State. Commun. **169**, 10–13 (2013)